



# Dual-field-of-view high-spectral-resolution lidar: Simultaneous profiling of aerosol and water cloud to study aerosol–cloud interaction

Nanchao Wang<sup>a,1</sup>, Kai Zhang<sup>a,1</sup>, Xue Shen<sup>a,1</sup>, Yuan Wang<sup>b</sup>, Jing Li<sup>c</sup>, Chengcai Li<sup>c</sup>, Jietai Mao<sup>c</sup>, Aleksey Malinka<sup>d</sup>, Chuanfeng Zhao<sup>e</sup>, Lynn M. Russell<sup>f</sup>, Jianping Guo<sup>g</sup>, Silke Gross<sup>h</sup>, Chong Liu<sup>a,i</sup>, Jing Yang<sup>a</sup>, Feitong Chen<sup>a</sup>, Lingyun Wu<sup>a</sup>, Sijie Chen<sup>a</sup>, Ju Ke<sup>a</sup>, Da Xiao<sup>a</sup>, Yudi Zhou<sup>a,b</sup>, Jing Fang<sup>a</sup>, and Dong Liu<sup>a,i,2</sup>

Edited by Joseph Francisco, University of Pennsylvania, Philadelphia, PA; received June 10, 2021; accepted January 22, 2022

Aerosol–cloud interaction (ACI) is complex and difficult to be well represented in current climate models. Progress on understanding ACI processes, such as the influence of aerosols on water cloud droplet formation, is hampered by inadequate observational capability. Hitherto, high-resolution and simultaneous observations of diurnal aerosol loading and cloud microphysical properties are challenging for current remote-sensing techniques. To overcome this conundrum, we introduce the dual-field-of-view (FOV) high-spectral-resolution lidar (HSRL) for simultaneously profiling aerosol and water cloud properties, especially water cloud microphysical properties. Continuous observations of aerosols and clouds using this instrument, verified by the Monte Carlo simulation and coincident observations of other techniques, were conducted to investigate the interactions between aerosol loading and water cloud microphysical properties. A case study over Beijing highlights the scientific potential of dual-FOV HSRL to become a significant contributor to the ACI investigations. The observed water cloud profiles identify that due to air entrainment its vertical structure is not perfectly adiabatic, as assumed by many current retrieval methods. Our ACI analysis shows increased aerosol loading led to increased droplet number concentration and decreased droplet effective radius—consistent with expectations—but had no discernible increase on liquid water path. This finding supports the hypothesis that aerosol-induced cloud water increase caused by suppressed rain formation can be canceled out by enhanced evaporation. Thus, these observations obtained from the dual-FOV HSRL constitute substantial and significant additions to understanding ACI process. This technique is expected to represent a significant step forward in characterizing ACI.

aerosol–cloud interaction | water clouds | high-spectral-resolution lidar | dual-field-of-view lidar

Aerosol–cloud interaction (ACI) is a crucial aspect of atmospheric research and one of the primary sources of uncertainties in climate predictions (1–3). To assess the credibility of climate projections, it is imperative to improve our understanding of how aerosols interact with clouds (4–6). It has been well known that aerosols can serve as cloud condensation nuclei (CCN) to form cloud droplets, which can further influence the initiation of precipitation (7). However, quantifying the impact of natural and anthropogenic aerosols on the growth and the evolution of water clouds is still challenging (8, 9). The short lifetime, high temporal variability, and complex vertical structure of water cloud layers lead to a major difficulty for ACI studies (3, 10, 11). Despite the advances in the characterization of ACI by ground-based measurements (12–21), satellite retrieved products (22–25), and airborne in situ measurements (26–28), uncertainties remain in the effects of the aerosols on the water cloud properties. The reason for this gap in our knowledge is closely linked to the inadequate observations of the water cloud microphysical properties under various aerosol conditions (3). Current satellites can estimate cloud properties but not the typical aerosol nucleation region beneath clouds (22–25). Moreover, they also bring challenges for ACI studies that the typical revisit time of satellite-based sensors is much longer than the temporal scales of cloud variability (29, 30). Quintessential ground-based remote-sensing techniques for retrieving cloud properties, such as the cloud radar and the microwave radiometer, cannot provide simultaneous aerosol observations for ACI studies. Therefore, ground-based measurements commonly combine those with other remote-sensing or in situ aircraft instruments for characterizing aerosol loading beneath clouds (12–20). However, given the high variability of clouds, differences in perspective or mismatched sampling in space and time would raise uncertainty and bias in the characterization of ACI (15).

Lidar, a powerful tool for profiling optical properties of aerosols and clouds, has been widely used in atmospheric studies (31–33). Yet, further progress with lidar-based

## Significance

Aerosol–cloud interaction affects the cooling of Earth's climate, mostly by activation of aerosols as cloud condensation nuclei that can increase the amount of sunlight reflected back to space. But the controlling physical processes remain uncertain in current climate models. We present a lidar-based technique as a unique remote-sensing tool without thermodynamic assumptions for simultaneously profiling diurnal aerosol and water cloud properties with high resolution. Direct lateral observations of cloud properties show that the vertical structure of low-level water clouds can be far from being perfectly adiabatic. Furthermore, our analysis reveals that, instead of an increase of liquid water path (LWP) as proposed by most general circulation models, elevated aerosol loading can cause a net decrease in LWP.

Author contributions: N.W. and D.L. designed research; X.S., C. Liu, J.Y., F.C., L.W., S.C., J.K., D.X., and J.F. performed research; K.Z., A.M., and Y.Z. contributed new reagents/analytic tools; N.W., Y.W., J.L., C. Li, J.M., A.M., C.Z., L.M.R., J.G., S.G., and D.L. analyzed data; N.W. and K.Z. wrote the paper; and X.S. provided validation data.

The authors declare no competing interest.

This article is a PNAS Direct Submission.

Copyright © 2022 the Author(s). Published by PNAS. This open access article is distributed under [Creative Commons Attribution-NonCommercial-NoDerivatives License 4.0 \(CC BY-NC-ND\)](https://creativecommons.org/licenses/by-nc-nd/4.0/).

<sup>1</sup>N.W., K.Z., and X.S. contributed equally to this work.

<sup>2</sup>To whom correspondence may be addressed. Email: liudongopt@zju.edu.cn.

This article contains supporting information online at <https://www.pnas.org/lookup/suppl/doi:10.1073/pnas.2110756119/-DCSupplemental>.

Published March 2, 2022.

techniques for ACI studies is hampered by limited observations of the water cloud microphysical properties, mainly due to the difficulties of quantifying the multiple scattering within water clouds (34). The multiple scattering has a significant impact on the water cloud observations of the extinction as well as the depolarization ratio, which is related to the receiver field of view (FOV). In brief, a retrieval of water cloud microphysical properties for lidar-based techniques relies on utilizing different receiver FOVs to provide the necessary observations for characterizing the multiple-scattering effect caused by the water droplets (34, 35). The first multiple-FOV lidars were aimed at investigating the multiple-scattering effect and measured Mie scattering by water droplets (36). However, a complicated behavior of the Mie phase function makes the quantifying of the multiple scattering become an arduous task. It naturally leads to the use of Raman scattering of atmospheric nitrogen, which has an isotropic phase function practically in the backward direction, to allow developing a feasible algorithm for the retrieval of water cloud microphysical properties (35). Moreover, the dual-FOV Raman lidar technique for profiling cloud properties has been experimentally demonstrated (37). With this technique in conjunction with an incoherent Doppler lidar, the ACI findings have been obtained with an ACI index versus vertical air motion (21, 38). However, nitrogen Raman signals are so weak that the observations are usually restricted to nighttime hours, and the signal has to be averaged over tens of minutes to deliver reliable lidar products, while the typical temporal scale of cloud variability is much shorter than that (29). Recently, a dual-FOV polarization lidar technique was reported, which continued and further developed the concept of the dual-FOV Mie lidar (39). However, to assess ACI this method requires a priori assumptions about the lidar ratio and subadiabatic cloud conditions. The impact of the a priori assumptions on the aerosol and cloud retrievals has been widely discussed (10, 40, 41). In general, all existing multiple-FOV lidar-based techniques have their advantages and also limitations.

To overcome this conundrum, a dual-FOV high-spectral-resolution lidar (HSRL) technique for profiling aerosol and cloud properties simultaneously is introduced here. It provides lateral observations of aerosols and clouds with high vertical and temporal resolutions during daytime and nighttime. Neither assumptions on thermodynamic conditions nor lidar ratio are required. This work benefited from the range-resolved observations of water clouds with high resolution, revealing that the observed profiles of low-level water cloud microphysical properties are not perfectly adiabatic as assumed by many current retrievals (42–46). Furthermore, the ACI analysis supports the hypothesis that aerosol-induced water decrease by enhanced evaporation can cancel out the increase caused by suppressed rain formation (6, 47), while most current global general circulation models (GCMs) suggest that increased aerosol loading typically causes increased cloud water content (19, 48). Thus, these observations obtained from the dual-FOV HSRL can constitute a substantial and significant addition to our understanding of ACI studies. We believe that this versatile system will not only benefit the quality monitoring of aerosol and cloud properties but also serve as a powerful tool for ACI studies.

## Results and Discussion

**Field Campaign and Dual-FOV HSRL System.** A dual-FOV HSRL system developed by Zhejiang University (ZJU) was operated in Beijing, China, from 25 October 2020 to 12 December 2020. The location of this field campaign is shown in *SI Appendix, Fig. S1*. Continuous observations of aerosols and clouds were conducted

near the Meteorological Bureau of Yanqing District (i.e., YQ site). Subsequently, we performed coincident observations (Data Quality Check) with cloud radar, Raman lidar, and a sun photometer to validate our results at Peking University (i.e., PKU site). Compared to typical single-FOV HSRL, the dual-FOV HSRL system equips an additional molecular channel with a different receiver FOV to characterize the multiple-scattering effect of water clouds. Elastic molecular scattering measured with the HSRL has similar angular behavior of the phase function to that of Raman scattering, thus allowing profiling of cloud microphysical properties without assuming thermodynamic conditions if the information on molecular scattering from dual FOVs is available (21, 37). At the same time the molecular signal measured with the dual-FOV HSRL is much stronger than the Raman signal, which enables us to profile aerosol and cloud properties during daytime and nighttime with high vertical and temporal resolutions for ACI studies. The development of our single-FOV HSRL system has been described in previous work (40); hence, only the general descriptions are given in *SI Appendix, Text S1*. *SI Appendix, Table S1* summarizes the general specifications of the dual-FOV HSRL configuration.

Due to the complex and combined influences of meteorological and aerosol-related aspects on cloud properties and evolution detailed in Fig. 1*A*, strong efforts regarding field observations of aerosol and cloud properties with high resolution are imperative (3). Therefore, it is fairly appealing to simultaneously profile the properties of aerosols and clouds with this lidar technique for understanding their interactions. The internal view and the schematic diagram of this lidar system are shown in Fig. 1*B* and *C*, respectively. The data analysis scheme about how to obtain the required observations of aerosol and water cloud properties is depicted in *SI Appendix, Text S2* and Fig. S2. The water cloud layers excluded from aerosols and ice clouds would be selected after the classification for the retrievals of cloud optical and microphysical properties, e.g., cloud extinction ( $\alpha_c$ ), cloud droplet effective radius ( $r_e$ ), cloud droplet number concentration ( $N_d$ ), and liquid water content (LWC), etc. The retrieval of water cloud microphysical properties is an iterative process based on a quasi-single-scattering analytical (QSA) model and an optimal estimation method, whose refinement is provided in Materials and Methods. Note that  $N_d$  cannot be retrieved from the lidar profile directly; instead, it is estimated to be proportional to the product of  $\alpha_c$  and  $r_e^{-2}$  (*SI Appendix, Text S3*). The optimization of lidar configuration and the determination of resolution follow the procedures in *SI Appendix, Texts S4* and *S5*.

**Data Quality Check.** Assessing the performance of dual-FOV HSRL for ACI studies is inherently difficult since there is little underlying truth in the practical cases. Quantitative tests for data quality were performed mainly by evaluating the retrieval of aerosol and cloud properties. Even a single-FOV HSRL can provide reliable observations of aerosol optical properties. Therefore, we would be more concerned about the data quality of water cloud microphysical properties. In this case, we conducted comparisons directly with the aerosol optical depth (AOD) derived from a sun photometer at daytime and aerosol extinction derived from a single-FOV Raman lidar at nighttime to verify the aerosol measurements from the dual-FOV HSRL. These results agree reasonably well (5.02 and 0.26% corresponding to AOD and aerosol extinction in terms of mean bias error, respectively), showing high quality of the aerosol products in *SI Appendix, Fig. S3*. Hereafter, we focus on the performance evaluation of the water cloud microphysical properties retrieval based on the dual-FOV HSRL.

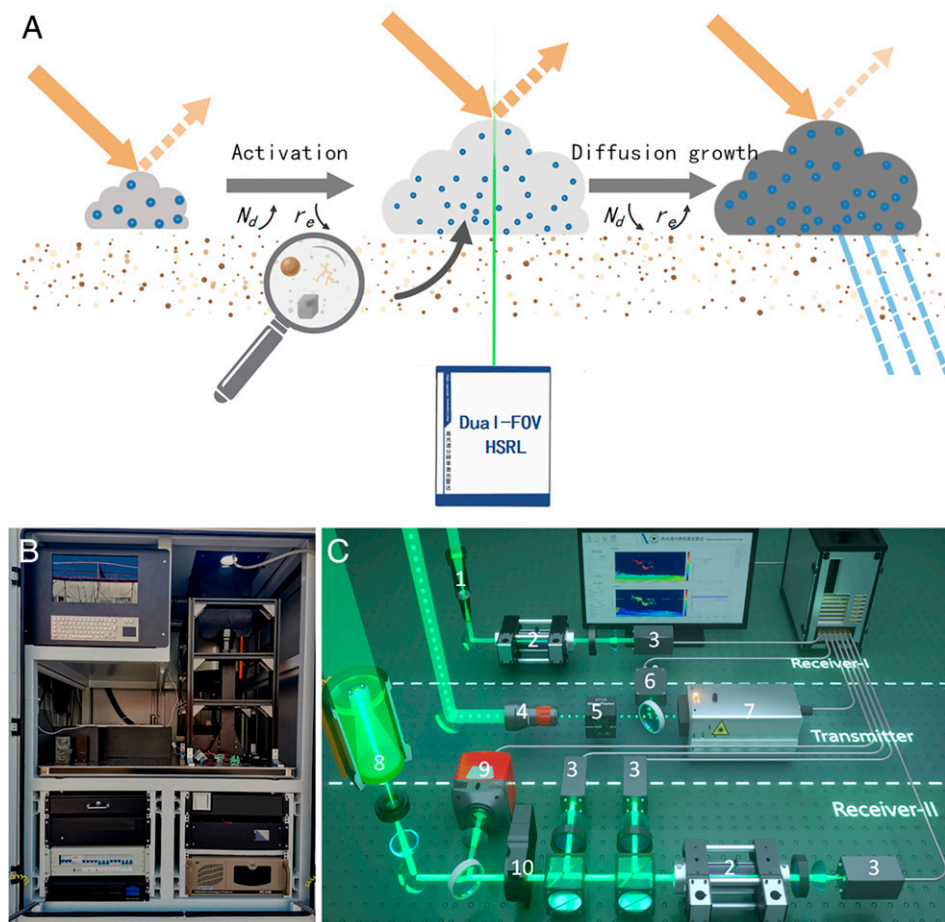


**Fig. 1.** Observational scheme of using the dual-FOV HSRL system to investigate the ACI. The ground-based lidar system performs continuous measurements of aerosols and clouds and conducts ACI analysis between aerosol loading and water cloud microphysical properties (cloud droplet number concentration  $N_d$ , effective radius  $r_e$ , liquid water content, etc.). (A) ACI can be analyzed based on temporal changes of the retrieved properties during 1) CCN activation of aerosol particles, leading to increasing  $N_d$ , decreasing  $r_e$ , and the resulting increase of solar reflectance and 2) diffusional growth of cloud droplets, enhancing condensational growth processes and enlarging particle sizes, and eventual precipitation through the mechanism of collision and coalescence. (B) The internal view of the dual-FOV HSRL system. (C) The schematic diagram of the dual-FOV HSRL system (see *SI Appendix, Text S1* for further description): 1, Kepler telescope; 2, iodine vapor cell; 3, detector; 4, beam expander; 5, Glan-Taylor prism; 6, power meter; 7, laser; 8, Schmidt-Cassegrain telescope; 9, camera; and 10, half-wave plate.

First, to investigate the feasibility and the uncertainty of the water cloud microphysical properties retrieval, a Monte Carlo (MC) model was employed here, as detailed in *SI Appendix, Text S4*. The simulated lidar profiles corresponding to the given microphysical properties of water clouds were computed using MC simulation and then used as input for the retrieval algorithm. Similar simulations for assessing the performance of retrieving cloud properties also can be found in other works (39, 49). In this simulation,  $r_e$  of the water cloud ranges from 6 to 18  $\mu\text{m}$ , while LWC varies from 0.05 to 0.45  $\text{gm}^{-3}$  to represent various cloud scenarios (homogeneous clouds for the sake of simplicity). The thickness of the water clouds with a cloud base height at 2 km was set to 150 m. Attenuated backscattering profiles with Poisson noise were then obtained assuming two different receiver FOVs of 1.0 and 2.0 mrad, respectively. Fig. 2 *A* and *B* shows the complete comparison from the 49 coincident cases in the simulation. In addition to comparing with the true values, we also assess the applicability of the retrieval algorithm in noisy conditions (Poisson noise in these cases). As can be seen, the  $r_e$  values obtained with the retrieval are in good agreement with the true values almost within  $\pm 30\%$  uncertainty, while the retrieved LWC values slightly exceed  $\pm 30\%$  error under high LWC conditions. The particular reason for this circumstance is that the retrieval of LWC is related to not only  $r_e$  but also  $\alpha_c$ , which

can be referred to in *SI Appendix, Text S3*. Similar simulations were done in *SI Appendix, Text S6*, but with different cloud-base height, different initialization of the retrieval, etc. Despite the different assumptions, the performances of the retrieval remain similar. There are multiple reasons for the noticeable biases that appeared with high values of  $r_e$  or LWC. The main reason is that high extinction coefficients induced by large cloud droplets (or high LWC values) attenuate the backscattering lidar signal to the noise level swiftly, imposing higher uncertainty on the retrieval. Another reason is that this lidar configuration is not optimal for all conditions, especially large cloud droplets (or high LWC values), as detailed in *SI Appendix, Text S4*. A narrow FOV is preferred for achieving lower uncertainty when measuring large cloud droplets. Furthermore, it illustrates that the accuracy of the QSA model also deteriorates when multiple scattering is prominent (i.e., high LWC) (50), since the QSA model simplifies the treatment of multiple scattering by assuming it as a sum of multiple small-angle forward scattering and single backward scattering. All parameters used in the simulation are listed in *SI Appendix, Table S2*, which coincide with those in the practical dual-FOV HSRL system.

Next, to assess the practical performance of dual-FOV HSRL for water clouds, simultaneous observations with a 33.44-GHz cloud radar and dual FOV HSRL were conducted at the PKU site on 6 December 2020. The droplet size distribution was assumed

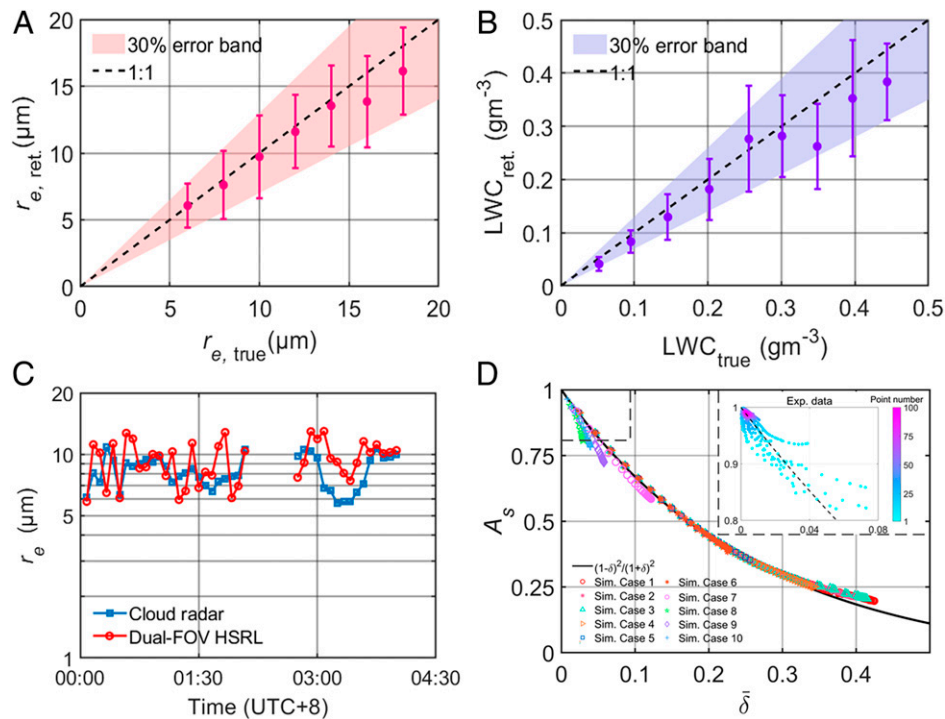


**Fig. 2.** Results of data quality check. (A and B) Comparisons of droplet  $r_e$  (A) and LWC (B) with the true values and the retrievals using MC simulations. Vertical lines stand for the SDs among several sets of retrievals using different  $r_e$  or LWC. (C) Comparison of the column mean values  $r_e$  with the cloud radar and the dual-FOV HSRL on 6 December 2020. Mean value of the bias is 8.31%. (D) The solid black line corresponds to the relationship between  $\bar{\delta}$  and  $A_S$  proposed by Hu et al. (52) according to the CALIOP observations. Comparisons of our MC computation and experiment data with the respective values predicted by the relationship are presented. The experimental data are shown in *Inset* separately.

for the retrieval of water cloud microphysical properties (51), since the actual distribution was not available. The observations not related directly to water cloud microphysical properties are shown in *SI Appendix, Fig. S4* for the sake of clarity, e.g., height versus time images of radar reflectivity and backscattering coefficient, etc. An in-depth explanation regarding the processing of this comparison is in *SI Appendix, Text S7*. Fig. 2C presents an example of point-to-point  $r_e$  comparison (column mean values) from the dual-FOV HSRL and the cloud radar. The bias presented in Fig. 2C falls within the acceptable uncertainty (8.31% in terms of mean bias) for the dual-FOV HSRL, considering that the cloud radar was measuring the water clouds along a slightly different path through the atmosphere (*SI Appendix, Fig. S4*). The good agreement of these lidar results with the respective cloud radar observations corroborates the quality of our retrieved cloud products. Note that potential uncertainties also exist within the radar retrievals (10).

Aside from the ground-based cloud radar, space-borne remote sensing could also provide similar observations of aerosols and clouds with the dual-FOV HSRL. Unfortunately, CloudSat has stopped providing radar data due to a failure of one of its three remaining reaction wheels since 27 August 2020. The data products of cloud properties from satellite passive remote sensing were also investigated to compare with our lidar observations, e.g., moderate resolution imaging spectroradiometer (MODIS) and visible infrared imaging radiometer (VIIRS) satellites. However, the revisit time from the satellite passive remote sensing was unsatisfactory to conduct a comprehensive comparison with the dual-FOV HSRL results (an example is shown in *SI Appendix, Fig. S5*). The explanation for those deviated results may involve several complicated factors, which are beyond the scope of this paper.

Therefore, we turn to verifying the statistical relationship derived from satellite observations, which is related to the water

cloud properties. For instance, Hu et al. (52) investigated the relationship between the ratio of the accumulated depolarization ratio ( $\bar{\delta}$ ) and the accumulated single-scattering fraction ( $A_S$ ) at 532 nm, which had been widely adopted in the analysis of water clouds from cloud-aerosol lidar with orthogonal polarization (CALIOP) measurements. Here, we extended the validation efforts to the MC simulation and the dual-FOV HSRL observations that provide comprehensive properties of water clouds in Fig. 2D. A great number of data points are available owing to 10 different cloud scenarios of the MC simulation and the extensive dual-FOV HSRL data products with high resolution for this comparison. The detailed parameters of the cloud scenarios used in the MC simulation are listed in *SI Appendix, Table S3*. The experiment results from the dual-FOV HSRL observations are displayed in Fig. 2D, *Inset* separately, and the other results are from the MC simulation. The relationship between  $\bar{\delta}$  and  $A_S$ , which corresponds to the solid black line in Fig. 2D, is in good agreement with the MC simulation and lidar observations. The  $\bar{\delta}$  values of the experimental observations are relatively low, shown in Fig. 2D, since the multiple-scattering effect would be much weaker due to the limited FOV footprint of the low-level water clouds from the ground-based lidar depolarization observations.

**Selected Case Study.** By design, the dual-FOV HSRL system observed nearly continuous cloudy weather over the YQ site on 14 November 2020. Fig. 3A–C provides an overview of the aerosols and the layered clouds from the lidar observations, consisting of backscattering coefficient, depolarization ratio, and feature classification. Complex cloudy conditions were observed, involving upper tropospheric ice clouds (phase 1), midlevel mixed-phase supercooled clouds (phase 2), and low-level water clouds (phase 3). Ice clouds extending from  $\sim 7$  to 9 km above ground were observed from midnight to 03:40 local time (LT). A

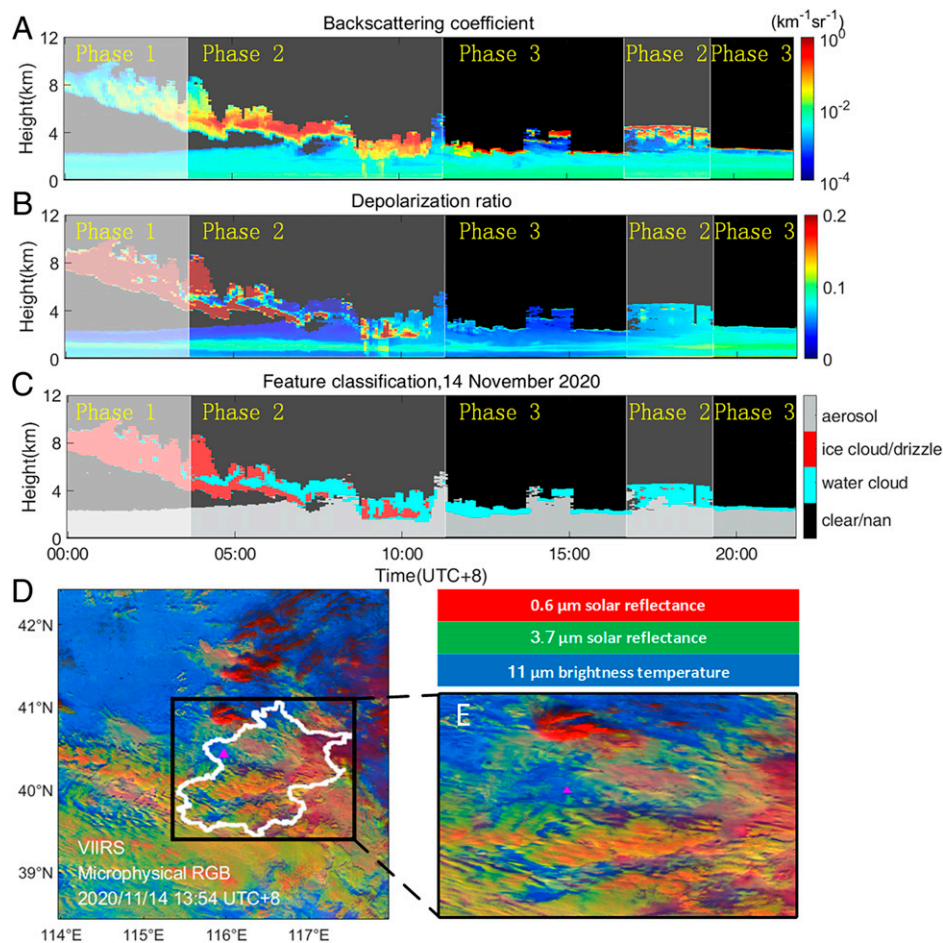


**Fig. 3.** Ground-based dual-FOV HSRL and space-borne passive remote-sensing observations on 14 November 2020 over Beijing YQ site. (A and B) Backscattering coefficient (A) and depolarization ratio (B) observed with the dual-FOV HSRL. (C) Feature classification of aerosol and cloud layers based on the lidar observations. (D) Pseudocolor RGB image from VIIRS observations on 14 November 2020, 13:54 LT. The pink triangle indicates the location of the YQ site, and the white line marks the border of Beijing City. (E) Same as D, but showing a detailed image around the YQ site.

high depolarization ratio of ice clouds was observed with values of above 0.20 due to the strong light depolarization caused by ice crystals shown in Fig. 3B. Later in the early morning, the ice clouds transformed into a mixed-phase cloud layer and produced precipitation, mostly in the form of drizzle. The mixed-phase clouds were observed at about 3 to 8 km above the ground, similar to the coexistence of a supercooled liquid and ice layer reported by our HSRL system (40). The depolarization ratio of the mixed-phase clouds is higher, pointing to the presence of ice particles. Since at the moment the retrieval of microphysical properties is applicable to pure water clouds, it is necessary to identify observation periods that are not contaminated by ice crystals (SI Appendix, Text S2). For instance, the observations during the time period from 16:40 to 19:15 LT may not be suitable for our algorithm, since the presence of multiple peaks in the vertical structure of the backscattering coefficient and depolarization ratio indicates that it should be identified as mixed-phase clouds. The observation period consisting of pure water cloud layers is labeled as phase 3 in Fig. 3 A–C, which is mainly discussed in the following section. The backscattering coefficient of the water clouds was significantly higher, shown in Fig. 3A, verifying the presence of relatively large concentrations or sizes of droplets within the clouds.

To further confirm the identification of the cloud phase, the overview of the synoptic situation around Beijing over central China with the widespread cloudiness is shown in Fig. 3D at 13:54 LT. The color scheme was selected to enhance the understanding

of the cloudy condition (53). In this work, the red-green-blue (RGB) compositions were modulated by visible reflectance (red), solar reflectance (green), and brightness temperature (blue) of VIIRS bands centered at 0.6, 3.7, and 11  $\mu\text{m}$ , respectively. Fig. 3E provides a detailed pseudocolor RGB image around the YQ site. The pink triangles in Fig. 3 D and E indicate the location of the YQ site in northwestern Beijing. Since solar reflectance is roughly inversely proportional to the effective radius when LWC is fixed, and brightness temperature is inversely proportional to height, Fig. 3E shows that, at the time of overpass, the test site is surrounded by relatively low-level clouds with small effective radius. There are sparse high-level clouds to the north of the site in full red, which may not be observed by the ground-based lidar. All observations from satellite images indicate that this is owing to the low-level warm water clouds over the YQ site, which coincides with lidar observations during that time.

Hindered by the variation of the cloud properties, the method of deriving the  $ACI_N$  parameter based on the relative change in  $N_d$  along with the aerosol loading in this work is applicable to a single continuous cloud layer with assumed uniform shape of droplet size distribution (SI Appendix, Text S3). Thus, only the long-lasting water cloud layer from 2.5 to 2.8 km height observed over several hours from 19:15 to 22:00 LT was selected to provide an example to investigate the cloud properties. Fig. 4 A and B shows the height versus time images of  $r_e$  and LWC with resolution of 5 min and 7.5 m retrieved from the dual-FOV HSRL during the selected observation period. The column mean

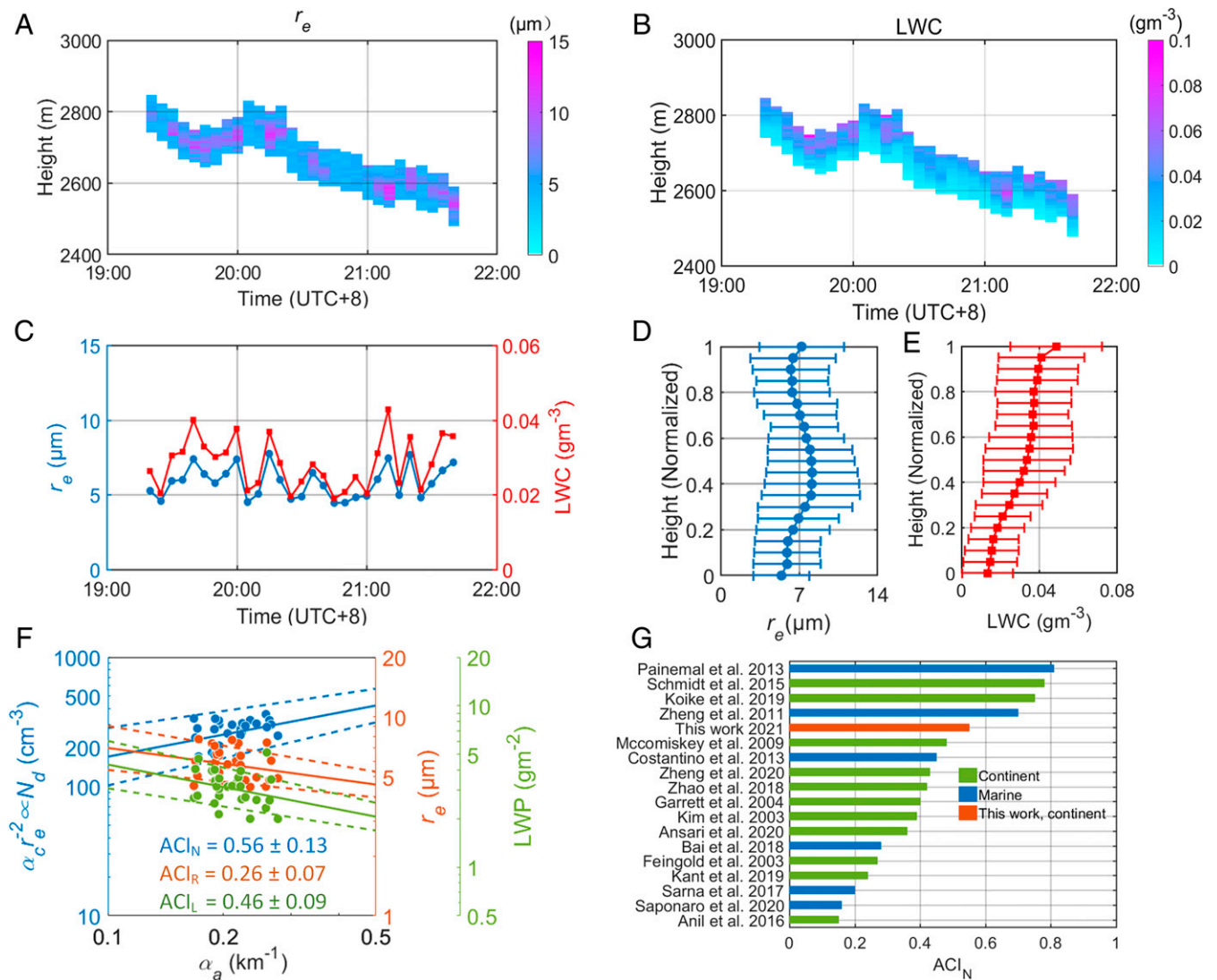


**Fig. 4.** Dual-FOV HSRL observations of water cloud microphysical properties. (A and B) Time versus height image of  $r_e$  (A) and LWC (B) with resolution of 7.5 m and 5 min retrieved from the dual-FOV HSRL. (C) The column mean value of  $r_e$  (blue) and LWC (red). (D and E) The retrievals of  $r_e$  (D) and LWC (E) were presented as a function of normalized height to investigate the vertical structure of the low-level water cloud. The error bars indicate the uncertainties of the retrieved values regarding the measurement profiles. (F) Correlations of retrieved cloud properties and the extinction of aerosol proxy. The slopes of solid lines correspond to the ACI parameters of  $N_d$  (in blue),  $r_e$  (in red), and LWC LWP (in green), respectively. Note that the dashed lines denote the uncertainties of ACI parameters (SD) due to the retrieval error of cloud properties. (G) Collected  $ACI_N$  values from extensive literature in the past two decades, including this work (12–20, 22–28, 38).

values of  $r_e$  and LWC are shown in Fig. 4C. Note that there is a temporal fluctuation of the water cloud properties, which is a typical situation found in the observations of well-developed and preexisting liquid water cloud layers (15). Statistically, the dense water clouds varied  $r_e$  with the highest-occurring values around 5 to 8  $\mu\text{m}$ , and the LWC was around 0.02 to 0.04  $\text{g}/\text{cm}^3$ . The relatively low values of  $r_e$  often occur with high values of  $N_d$ . These properties are typical of nonprecipitating low-level water clouds in the polluted continental or marine environment (15, 18, 19).

We want to further demonstrate that the assumption of pure adiabatic conditions is unsuitable for retrieving low-level water cloud microphysical properties in some cases. The nearly adiabatic vertical profile has been the basis for satellite retrieval of cloud properties (41), since the direct satellite retrieval of natural vertical cloud structure is not available. However, the observed droplet  $r_e$  shows that the vertical structure of the selected cloud layer is far from being a perfectly adiabatic cloud layer. For the sake of clarity, the vertical structure of water cloud microphysical properties has

been investigated as functions of the cloud normalized height in Fig. 4D and E. LWC monotonically increased with height; however, the vertical profile of the droplet  $r_e$  shows an increase followed by a decrease with height. These features indicate that the entrainment of dry air into the cloud top causes the deviation of the water cloud microphysical properties from those expected of adiabatic ascending parcels (44). The outcome is a decrease in  $r_e$  over the cloud top, while  $N_d$  is conserved (SI Appendix, Fig. S6). Since the droplet sedimentation rate is inversely related to  $N_d$ , the proliferation of  $N_d$  in the entrainment zone at the cloud top (SI Appendix, Fig. S6) leads to the decrease of sedimentation flux (54). This decreased flux enhances two cooling mechanisms that promote the sinking of entrained air into this nocturnal nondrizzling cloud layer, that is, entrainment-induced evaporative cooling and longwave radiative cooling. The evaporative cooling from mixing of cloud top and above cloud air as well as the cloud top radiative cooling further enhances the cloud top entrainment. Both of them constitute a hybrid positive feedback between  $N_d$  and the entrainment rate—the higher the entrainment rate is, the higher

$N_d$  will be, and vice versa (55). Consequently, it naturally leads to the deviation from the expected adiabatic profiles, especially for the cloud top, which is also frequently observed in the vertical profile of continental and maritime convective clouds (42–46). These facts suggest that the vertical structure of low-level water clouds should not be regarded simply as perfectly adiabatic, even though adiabatic or subadiabatic assumptions have been widely adopted in passive remote-sensing algorithms to retrieve cloud products simply because of the lack of availability of ambient cloud profiles (29). The bias of the cloud vertical structure would impose further uncertainty on those retrievals with an a priori assumption of adiabatic profiles (41), since the assumption may not be tenable when a droplet collision and coalescence process, droplet evaporation, or air entrainment occurs (56).

To quantify the aerosol effect on cloud properties, ACI parameters are adopted to describe the relative change of cloud properties with the aerosol loading (13). A larger ACI parameter usually indicates a stronger response to aerosols by the respective cloud properties. The aerosol extinction rather than CCN is employed here to characterize the aerosol loading in this correlation analysis, since the aerosol extinction ( $\alpha_a$ ) is directly retrieved from the dual-FOV HSRL with low uncertainty. Despite the complex cloud structures, processes, and features, we calculate the correlation between the derived column mean cloud properties and measured aerosol extinction from 400 to 600 m below the cloud base. A distance of 400 to 600 m from nucleated aerosols to the cloud base was chosen to prevent water-uptake effects influencing aerosol extinction (38, 56). To better illustrate the rationale of the selected height range, the height versus time image of the extinction coefficient (multiple-scattering affected) with temporal resolution of 1 min and vertical resolution of 7.5 m, including the selected cloud layer and the aerosols beneath clouds, is depicted in *SI Appendix, Fig. S9*. A typical structure of the nocturnal boundary layer is clearly presented—a stable shallow surface mixing layer below 1.25 km and above a residual aerosol layer. The selected height range of aerosol extinction coefficients is within the residual layer and is in close proximity to the investigated cloud layer with sufficient signal-to-noise ratio. The residual layer is more likely to interact with the low-level water clouds rather than the well-mixed layer near the ground and similarly for the upper layer of the residual layer. To roughly estimate the impact of the retrieved uncertainties of cloud properties on ACI parameters, a MC method is adopted here to distort the retrievals of cloud properties within uncertainties shown in Data Quality Check. For every single point of the cloud properties, the artificial distortion would repeat 10,000 times and then recalculate the corresponding ACI parameters at the same time. Thus, the uncertainties of ACI parameters could be assessed by the SDs of ACI parameters derived from distorted input data.

In general, the increased  $N_d$  and the reduced  $r_e$  change with increased aerosol loading in Fig. 4*F* as expected. The relationship between cloud droplet  $N_d$  and  $\alpha_a$  in this work is expressed in forms of the  $ACI_N$  parameter around  $0.56 \pm 0.13$ . As for the cloud droplet  $r_e$ , the  $ACI_R$  index is  $0.26 \pm 0.07$ , thereby emphasizing a relatively high sensitivity of cloud droplet  $r_e$  response. Note that values of  $ACI_R$  theoretically range from 0 to 0.33. Such a high  $ACI_R$  value indicates a relatively strong evaporation within water clouds under low liquid-water-path (LWP) conditions, which is consistent with the established study derived from a long-term ACI analysis from an atmospheric radiation measurement (ARM) ground-based site (19). Thus a large number of small radius droplets, as can be seen in the observations, compete with each other for limited water supply to enhance the increasing of  $ACI_R$ . In regard to the LWP, most studies

suggest that smaller cloud droplets (namely, higher aerosol loading within the aerosol nucleation region) decreasing the efficiency of collision–coalescence processes usually lead to a significant increase in LWP (19, 48). But this common result in most current GCMs follows a contentious debate, in recent years, that the LWP can also decrease owing to some dynamical feedbacks (e.g., cloud top entrainment, aerosol-enhanced evaporation, etc.) (6, 47). In this ACI analysis, no statistically significant increase in LWP is detectable. Instead of a strong increase, increased aerosol loading causes a net decrease in the corresponding values of LWP ( $ACI_L = 0.46 \pm 0.09$ ). Although this finding is consistent with ACI studies with negative LWP response to aerosols (6, 47, 57), the detailed feedback mechanisms are still unclear on whether or not the sign of the net effect of aerosols on LWP is positive. The LWP susceptibility is generally positive for water clouds with small  $N_d$  and large  $r_e$ , but is very likely negative for the opposite conditions (6). As aerosols usually covary with multiple environmental factors, identifying causality for changes in LWP in response to aerosols is challenging. Smaller cloud droplets resulting from increased aerosol concentrations decrease the efficiency of droplet collision–coalescence processes, extending the cloud lifetime and cloud coverage as well as postponing the initiation of precipitation (i.e., precipitation suppression or the “second indirect effect of aerosols”) (5). In contrast, there are two main feedback mechanisms to cause the decrease of LWP within the selected cloud layer. The first one is the sedimentation–entrainment feedback. The reduction of sedimentation flux, resulting from small  $r_e$  and increasing  $N_d$  associated with ACI, maintains large amounts of liquid water in the entrainment zone at cloud top (54). It leads to increases in evaporative cooling, radiative cooling, and entrainment rate at the cloud top under polluted conditions. A second feedback effect stems from the relatively large total surface area of small cloud droplets (at the same LWP condition) but with faster evaporation rates and intensified entrainment for similar meteorological conditions, known as the evaporation–entrainment feedback (55). The complex interplay of those mechanisms causes a net negative LWP susceptibility to aerosols in our observations. To put the aerosol effect on  $N_d$  from this case study into context with the other similar works, as did Schmidt et al. (38), we collected the available  $ACI_N$  values from extensive literature in the past two decades for comparison in Fig. 4*G* (12–20, 22–28, 38). Some other established results are not shown here for the sake of clarity. As can be seen, the reported physically meaningful  $ACI_N$  values cover almost the full range from 0 (no aerosol interaction) to 1 (linear increase with aerosol loading). The reasons for the wide range of the  $ACI_N$  values involve numerous aspects, e.g., geographical environment, conditions regarding aerosols and clouds, etc. The  $ACI_N$  value in this work indicates a moderate interaction of aerosols and cloud droplets as can be seen in Fig. 4*G*.

Nevertheless, it is noteworthy that the cloud samples and the time window are limited in this work compared to other publications. More samples of typical cloud scenarios will be accessed by using this instrument in future work, e.g., shallow convective clouds, stratocumulus, etc. Possibilities of further extending this technique to ice crystal and mixed-phase clouds will be considered. We will also try extending further capabilities under development to better quantify ACI process, e.g., vertical Doppler wind measurements, size distribution of nucleated aerosols retrieved from multiwavelength optical properties, atmospheric humidity information, etc. By employing reanalysis data, there are also potential insights for exploring the impact of meteorological conditions on ACI (55). Further progress on modeling the ACI process under different conditions will be achieved using this technique in the future.

## Materials and Methods

**Multiple-Scattering Model.** The multiple-scattering model is crucial for the retrieval of the water cloud microphysical properties, as a tool for simulating the lidar return profiles corresponding to the assumed cloud properties. The MC method has been widely used in the numerical simulation model for simulating lidar signals of water clouds including the multiple-scattering effect. This method transforms the generation of lidar signals into the interpretable processing of photon emission, scattering, and receiving. The standard MC method can simulate the lidar return profiles more accurately; however, it is quite time consuming for our proposed retrieval of the water cloud properties. Although semianalytical MC has been demonstrated to improve the computational efficiency (58), it is still not fast enough to meet the needs of our retrieval. Therefore, the MC method was used only to simulate the water cloud signals of the dual-FOV HSRL as the synthetic signals to validate our retrieval algorithm.

Considering the limitations of the MC method, an analytical model was developed for our retrieval algorithm directly instead of the MC method. The photons penetrated in cloud droplets contributing to the lidar signals primarily consist of those from multiple small-angle forward scattering and single backward scattering, which provides a feasible approximation for modeling the multiple-scattering effects (i.e., the QSA approximation) (50). The QSA approximation simplifies the modeling of the laser beam propagation process within clouds and allows one to simulate the lidar return signals efficiently. The analytical multiple-scattering model (i.e., the QSA model) offers us a solution to simulate water cloud lidar signals with high efficiency and relatively high accuracy, which is used as a forward model for the retrieval of water cloud properties.

The original QSA model is designed for Raman scattering (35, 37, 50); however, one can easily modify this model to generate attenuated backscattering signals of atmospheric molecular elastic scattering (i.e., Rayleigh scattering) with only a few modifications. First of all, it is simpler to simulate elastic scattering in comparison with Raman scattering, as elastic scattering involves no wavelength shift. Also, the cross-section of Rayleigh scattering is significantly larger than the cross-section of Raman scattering. Moreover, the Rayleigh phase function corresponding to molecular scattering should be employed, for which the analytical form can be given by (58)

$$P_m(\theta) = 3(1 + p \cos^2 \theta) / [4\pi(3 + p)],$$

with the polarization parameter  $p$ .

**Retrieval Scheme for Water Cloud Microphysical Properties.** This section briefly presents the algorithm for the retrieval of water cloud microphysical properties, utilizing lidar signals of two molecular channels with different receiver FOVs. In the beginning, the extinction from a narrow FOV channel is adopted as the initial value of  $\alpha_c$ . The droplet  $r_e$  of water clouds is considered to be a typical range from 4 to 20  $\mu\text{m}$ , and its initial value is set to 9  $\mu\text{m}$ . With the assumed values of  $\alpha_c$  and  $r_e$ , the simulated attenuated molecular backscattering lidar signals can be obtained:

$$\begin{aligned} \beta'_{S1}(z) &= F(\alpha_c(z), r_e(z), \text{FOV}_1), \\ \beta'_{S2}(z) &= F(\alpha_c(z), r_e(z), \text{FOV}_2), \end{aligned}$$

where the  $F$  symbol represents the forward physical processing to simulate the lidar signals by the QSA model; the FOV corresponds to the practical size of receiver FOV; the  $\beta'_{S1}(z)$  and  $\beta'_{S2}(z)$  are the simulated lidar signals from two molecular channels with different receiver FOVs; and the subscript 1 denotes the narrow FOV and the subscript 2 represents the wider one, respectively. Then the alternative solution could be generated by an iterative optimal estimation scheme. The iterative optimal estimation method attempts to retrieve  $\alpha_c$  and

$r_e$  by minimizing the distance between the simulated lidar profiles and the measured ones, which could be expressed as

$$\{\alpha_{c,ret}(z), r_{e,ret}(z)\} = \operatorname{argmin} \left\| \beta'_S(z) - \beta'_M(z) \right\|_2 = \operatorname{argmin} \psi,$$

where  $\beta'_M(z)$  represents the measured lidar signals;  $\psi$  could be referred to as the cost function. The gradient of the cost function could be written as

$$\nabla \psi = \left( \frac{\partial \psi}{\partial \alpha_c(z)}, \frac{\partial \psi}{\partial r_e(z)} \right).$$

Starting with the trial values  $\alpha_{c,k}(z)$  and  $r_{e,k}(z)$  as an example, the retrieved values could be generated to converge toward a minimum cost function by an iterative process:

$$\{\alpha_{c,k+1}(z), r_{e,k+1}(z)\} = \{\alpha_{c,k}(z), r_{e,k}(z)\} - \eta \cdot \nabla \psi,$$

where  $\eta$  is a hyperparameter to manage the step size and convergence rate. Since the convergence rate might be slow when the retrieved values are close to the true values, the iterative process would be stopped if the relative difference between measured lidar signals and simulated signals were within the predetermined thresholds. An intuitive illustration of the iterative optimal estimation is shown in *SI Appendix, Fig. S6*. Once the  $\alpha_c$  and  $r_e$  are retrieved, the  $N_d$  and the LWC can be estimated as

$$\begin{aligned} N_d &\propto \alpha_c r_e^{-2} (\text{cm}^{-3}), \\ \text{LWC} &= \frac{2}{3} \rho_w \alpha_c r_e (\text{gm}^{-3}), \end{aligned}$$

where the  $\rho_w$  is the water density. Thus, ACI parameters can be calculated to describe the relative change of cloud properties with the aerosol loading, as detailed in *SI Appendix, Text S3*.

**Data Availability.** The VIIRS data in Fig. 3 D and E can be freely accessed from <https://ncc.nesdis.noaa.gov/VIIRS/>. The ACI index data in Fig. 4G can be found in the corresponding references cited in this manuscript. All other study data are included in the article and/or *SI Appendix*.

**ACKNOWLEDGMENTS.** We specially acknowledge Dr. Daniel Rosenfeld (Hebrew University of Jerusalem) and Dr. Zongyin Yang (Zhejiang University) for their valuable comments to improve the manuscript. We acknowledge Dr. Lei Bi and Dr. Wushao Lin (Zhejiang University) for their great help on the cloud depolarization simulations. This study was supported by the National Key Research and Development Program of China (2016YFC0200700), the National Natural Science Foundation of China (41775023, 41925022), the Excellent Young Scientist Program of Zhejiang Provincial Natural Science Foundation of China (LR19D050001), Fundamental Research Funds for the Central Universities (2019FZJD011), the State Key Laboratory of Modern Optical Instrumentation Innovation Program (MOI2018ZD01), and the Belarusian State Research Program Photonics and Electronics for Innovations.

Author affiliations: <sup>a</sup>State Key Laboratory of Modern Optical Instrumentation, College of Optical Science and Engineering, Zhejiang University, Hangzhou 310000, China; <sup>b</sup>Division of Geological and Planetary Sciences, California Institute of Technology, Pasadena, CA 91109; <sup>c</sup>Department of Atmospheric and Oceanic Sciences, Laboratory for Climate and Ocean-Atmosphere Studies, School of Physics, Peking University, Beijing 100871, China; <sup>d</sup>Institute of Physics, National Academy of Sciences of Belarus, Minsk 220072, Belarus; <sup>e</sup>State Key Laboratory of Earth Surface Processes and Resource Ecology, College of Global Change and Earth System Science, Beijing Normal University, Beijing 100088, China; <sup>f</sup>Scripps Institution of Oceanography, University of California San Diego, La Jolla, CA 92093; <sup>g</sup>State Key Laboratory of Severe Weather, Chinese Academy of Meteorological Sciences, Beijing 100081, China; <sup>h</sup>Institut für Physik der Atmosphäre, Deutsches Zentrum für Luft und Raumfahrt, Oberpfaffenhofen 82234, Germany; and <sup>i</sup>International Research Center for Advanced Photonics, Zhejiang University, Hangzhou 310000, China

1. J. H. Seinfeld *et al.*, Improving our fundamental understanding of the role of aerosol-cloud interactions in the climate system. *Proc. Natl. Acad. Sci. U.S.A.* **113**, 5781–5790 (2016).
2. K. S. Carslaw *et al.*, Large contribution of natural aerosols to uncertainty in indirect forcing. *Nature* **503**, 67–71 (2013).
3. D. Rosenfeld, S. Sherwood, R. Wood, L. Donner, Atmospheric science. Climate effects of aerosol-cloud interactions. *Science* **343**, 379–380 (2014).

4. P. J. DeMott *et al.*, Predicting global atmospheric ice nuclei distributions and their impacts on climate. *Proc. Natl. Acad. Sci. U.S.A.* **107**, 11217–11222 (2010).
5. Y. Sato *et al.*, Aerosol effects on cloud water amounts were successfully simulated by a global cloud-system resolving model. *Nat. Commun.* **9**, 985 (2018).
6. V. Toll, M. Christensen, J. Quaas, N. Bellouin, Weak average liquid-cloud-water response to anthropogenic aerosols. *Nature* **572**, 51–55 (2019).



7. D. Rosenfeld *et al.*, Flood or drought: How do aerosols affect precipitation? *Science* **321**, 1309–1313 (2008).
8. A. McComiskey, G. Feingold, Quantifying error in the radiative forcing of the first aerosol indirect effect. *Geophys. Res. Lett.* **35**, L02810 (2008).
9. C. Zhao *et al.*, Aerosol characteristics and impacts on weather and climate over the Tibetan Plateau. *Natl. Sci. Rev.* **7**, 492–495 (2020).
10. C. Zhao *et al.*, Toward understanding of differences in current cloud retrievals of ARM ground-based measurements. *J. Geophys. Res. Atmos.* **117**, JD016792 (2012).
11. Y. Wang *et al.*, Impacts of long-range transport of aerosols on marine-boundary-layer clouds in the eastern North Atlantic. *Atmos. Chem. Phys.* **20**, 14741–14755 (2020).
12. G. Feingold, W. L. Eberhard, D. E. Veron, M. Previdi, First measurements of the Twomey indirect effect using ground-based remote sensors. *Geophys. Res. Lett.* **30**, 1287 (2003).
13. B. G. Kim, S. Schwartz, M. Miller, Q. Min, Effective radius of cloud droplets by ground-based remote sensing: Relationships to aerosol. *J. Geophys. Res.* **108**, 4740 (2003).
14. T. J. Garrett, C. Zhao, X. Dong, G. G. Mace, P. V. Hobbs, Effects of varying aerosol regimes on low-level Arctic stratus. *Geophys. Res. Lett.* **31**, L17105 (2004).
15. A. McComiskey *et al.*, An assessment of aerosol-cloud interactions in marine stratus clouds based on surface remote sensing. *J. Geophys. Res. Atmos.* **114**, D09203 (2009).
16. V. Anil Kumar *et al.*, Investigation of aerosol indirect effects on monsoon clouds using ground-based measurements over a high-altitude site in Western Ghats. *Atmos. Chem. Phys.* **16**, 8423–8430 (2016).
17. K. Sarna, H. W. J. Russchenberg, Monitoring aerosol–cloud interactions at the CESAR observatory in the Netherlands. *Atmos. Meas. Tech.* **10**, 1987–1997 (2017).
18. M. Koike *et al.*, Year-round in situ measurements of arctic low-level clouds: Microphysical properties and their relationships with aerosols. *J. Geophys. Res. Atmos.* **124**, 1798–1822 (2019).
19. X. Zheng *et al.*, Investigation of aerosol–cloud interactions under different absorptive aerosol regimes using Atmospheric Radiation Measurement (ARM) southern Great Plains (SGP) ground-based measurements. *Atmos. Chem. Phys.* **20**, 3483–3501 (2020).
20. K. Ansari, G. Pandithurai, A. Kumar, Role of droplet size classes on the cloud droplet spectral dispersion as observed over the Western Ghats. *Atmos. Res.* **246**, 105104 (2020).
21. J. Schmidt *et al.*, Dual-FOV Raman and Doppler Lidar studies of aerosol–cloud interactions: Simultaneous profiling of aerosols, warm–cloud properties, and vertical wind. *J. Geophys. Res. Atmos.* **119**, 5512–5527 (2014).
22. L. Costantino, F. M. Breon, Aerosol indirect effect on warm clouds over south-east Atlantic, from co-located MODIS and CALIPSO observations. *Atmos. Chem. Phys.* **13**, 69–88 (2013).
23. H. Bai, C. Gong, M. Wang, Z. Zhang, T. L'Ecuyer, Estimating precipitation susceptibility in warm marine clouds using multi-sensor aerosol and cloud products from a-train satellites. *Atmos. Chem. Phys.* **18**, 1763–1783 (2018).
24. S. Kant, J. Panda, R. Gautam, A seasonal analysis of aerosol–cloud–radiation interaction over Indian region during 2000–2017. *Atmos. Environ.* **201**, 212–222 (2019).
25. G. Saponaro *et al.*, Evaluation of aerosol and cloud properties in three climate models using MODIS observations and its corresponding COSP simulator, as well as their application in aerosol–cloud interactions. *Atmos. Chem. Phys.* **20**, 1607–1626 (2020).
26. X. Zheng *et al.*, Observations of the boundary layer, cloud, and aerosol variability in the southeast pacific near-coastal marine stratocumulus during vocals-rex. *Atmos. Chem. Phys.* **11**, 9943–9959 (2011).
27. D. Painemal, P. Zuidema, The first aerosol indirect effect quantified through airborne remote sensing during VOCALS-REX. *Atmos. Chem. Phys.* **13**, 917–931 (2013).
28. C. Zhao *et al.*, Negative aerosol–cloud relationship from aircraft observations over Hebei, China. *Earth Space Sci.* **5**, 19–29 (2018).
29. D. P. Grosvenor *et al.*, Remote sensing of droplet number concentration in warm clouds: A review of the current state of knowledge and perspectives. *Rev. Geophys.* **56**, 409–453 (2018).
30. Y. Wang, C. Zhao, Can MODIS cloud fraction fully represent the diurnal and seasonal variations at DOE ARM SGP and Manus sites? *J. Geophys. Res. Atmos.* **122**, 329–343 (2017).
31. D. Winker, W. Hunt, M. McGill, Initial performance assessment of CALIOP. *Geophys. Res. Lett.* **34**, L19803 (2007).
32. J. W. Hair *et al.*, Airborne high spectral resolution lidar for profiling aerosol optical properties. *Appl. Opt.* **47**, 6734–6752 (2008).
33. R. Engelmann *et al.*, The automated multiwavelength Raman polarization and water-vapor lidar pollyx: The next generation. *Atmos. Meas. Tech.* **9**, 1767–1784 (2016).
34. I. Veselovskii *et al.*, Information content of data measured with a multiple-field-of-view lidar. *Appl. Opt.* **45**, 6839–6848 (2006).
35. A. V. Malinka, E. P. Zege, Possibilities of warm cloud microstructure profiling with multiple-field-of-view Raman lidar. *Appl. Opt.* **46**, 8419–8427 (2007).
36. L. R. Bissonnette, D. L. Hutt, Multiple scattering lidar. *Appl. Opt.* **29**, 5045–5046 (1990).
37. J. Schmidt, U. Wandinger, A. Malinka, Dual-field-of-view Raman lidar measurements for the retrieval of cloud microphysical properties. *Appl. Opt.* **52**, 2235–2247 (2013).
38. J. Schmidt, A. Ansmann, J. Bühl, U. Wandinger, Strong aerosol–cloud interaction in altocumulus during updraft periods: Lidar observations over central Europe. *Atmos. Chem. Phys.* **15**, 10687–10700 (2015).
39. C. Jimenez *et al.*, The dual-field-of-view polarization lidar technique: A new concept in monitoring aerosol effects in liquid-water clouds – Theoretical framework. *Atmos. Chem. Phys.* **20**, 15247–15263 (2020).
40. N. Wang *et al.*, Development of ZJU high-spectral-resolution lidar for aerosol and cloud: Feature detection and classification. *J. Quant. Spectrosc. Radiat. Transf.* **261**, 107513 (2021).
41. D. Merk, H. Deneke, B. Pospichal, P. Seifert, Investigation of the adiabatic assumption for estimating cloud micro- and macrophysical properties from satellite and ground observations. *Atmos. Chem. Phys.* **16**, 933–952 (2016).
42. F. Burnet, J. L. Brenguier, Observational study of the entrainment–mixing process in warm convective clouds. *J. Atmos. Sci.* **64**, 1995–2011 (2007).
43. E. Freud, D. Rosenfeld, J. R. Kulkarni, Resolving both entrainment–mixing and number of activated CCN in deep convective clouds. *Atmos. Chem. Phys.* **11**, 12887–12900 (2011).
44. M. J. Beals *et al.*, Holographic measurements of inhomogeneous cloud mixing at the centimeter scale. *Science* **350**, 87–90 (2015).
45. R. C. Braga *et al.*, Further evidence for CCN aerosol concentrations determining the height of warm rain and ice initiation in convective clouds over the Amazon basin. *Atmos. Chem. Phys.* **17**, 14433–14456 (2017).
46. K. J. Sanchez *et al.*, Measurement report: Cloud processes and the transport of biological emissions affect southern ocean particle and cloud condensation nuclei concentrations. *Atmos. Chem. Phys.* **21**, 3427–3446 (2021).
47. F. F. Malavelle *et al.*, Strong constraints on aerosol–cloud interactions from volcanic eruptions. *Nature* **546**, 485–491 (2017).
48. K. Suzuki, G. L. Stephens, M. D. Lebsock, Aerosol effect on the warm rain formation process: Satellite observations and modeling. *J. Geophys. Res. Atmos.* **118**, 170–184 (2013).
49. D. P. Donovan, H. Klein Baltink, J. S. Henzing, S. R. de Roode, A. P. Siebesma, A depolarisation lidar-based method for the determination of liquid–cloud microphysical properties. *Atmos. Meas. Tech.* **8**, 237–266 (2015).
50. A. V. Malinka, E. P. Zege, Analytical modeling of Raman lidar return, including multiple scattering. *Appl. Opt.* **42**, 1075–1081 (2003).
51. C. Zhao *et al.*, MMCR-based characteristic properties of non-precipitating cloud liquid droplets at Naqu site over Tibetan Plateau in July 2014. *Atmos. Res.* **190**, 68–76 (2017).
52. Y. Hu *et al.*, Simple relation between lidar multiple scattering and depolarization for water clouds. *Opt. Lett.* **31**, 1809–1811 (2006).
53. D. Rosenfeld *et al.*, High-resolution (375 m) cloud microstructure as seen from the NPP/VIIRS satellite imager. *Atmos. Chem. Phys.* **14**, 2479–2496 (2014).
54. C. S. Bretherton, P. N. Blossey, J. Uchida, Cloud droplet sedimentation, entrainment efficiency, and subtropical stratocumulus albedo. *Geophys. Res. Lett.* **34**, L03813 (2007).
55. E. Gryspeerd *et al.*, Constraining the aerosol influence on cloud liquid water path. *Atmos. Chem. Phys.* **19**, 5331–5347 (2019).
56. C. Jimenez *et al.*, The dual-field-of-view polarization lidar technique: A new concept in monitoring aerosol effects in liquid-water clouds – Case studies. *Atmos. Chem. Phys.* **20**, 15265–15284 (2020).
57. E. Jung *et al.*, Precipitation effects of giant cloud condensation nuclei artificially introduced into stratocumulus clouds. *Atmos. Chem. Phys.* **15**, 5645–5658 (2015).
58. Q. Liu *et al.*, A semianalytic Monte Carlo simulator for spaceborne oceanic LiDAR: Framework and preliminary results. *Remote Sens.* **12**, 2820 (2020).